Hai-bo Li · Shun-chao Qi · Hao Chen · Hai-mei Liao · Yi-fei Cui · Jia-wen Zhou

Mass movement and formation process analysis of the two sequential landslide dam events in Jinsha River, Southwest China

Abstract The formation of the landslide dam is believed to be case-specific and closely related to the dynamics of failure mass movement and river bed topography. This study focuses on two massive landslides, which blocked the Jinsha River twice on October 11 and November 3, 2018, respectively. The unique feature of these two sequential events was that the remnant of the 1st landslide dam body after break had a significant influence on the formation and shape of the 2nd landslide dam. Multiple methods were used to investigate landslides triggering factors and formation mechanism of these two landslide dams, including traditional field investigation, satellite remote sensing, and unmanned aerial vehicle (UAV) 3D image technology. After long-term creeping deformation under gravitational and hydrological effects, the first failure eventually occurred due to the short-term heavy rainfall in early October 2018. With a high speed along the steep slide bed, the failure mass of the 1st landslide rushed towards the opposite (left) bank of the Jinsha River, while the failure mass of 2nd landslide mainly accumulated at the toe of the slope (right bank) as a result of obstruction from the remaining body of the 1st landslide dam after overflowing. Another important observation is the scraping and entrainment effect on the 2nd landslide; consequently, the volume of the failure mass, which was about 2.0×10^6 m^3 at source area based on UAV data, increased significantly to more than 6.0×10^6 m^3. This substantially enlarged the volume of the new landslide dam with an unexpected height; thus, overflowing was not possible without manual excavation. An additional investigation implies that the Baige remnant slope is likely to fail again with considerable failure mass. These analyses presented in the paper indicate that multiple occurrences of landslides can significantly increase the risks associated with the compound landslide dams, considering also the volume amplification effect. Thus, timely measures should be carried out to reduce the unexpected devastating consequences prior to possible re-occurrence of landslide.

Keywords The Baige landslide dam · Multiple landslide · Mass movement · Formation process · Sliding volume amplification effect

Introduction

Landslide dams are common geological disasters in mountainous areas and are defined as permanent or ephemeral interruptions in a river course by landslide deposits (Costa and Schuster 1988; Zhou et al. 2016). Landslide dams pose serious threats to infrastructures near the dam and to inhabitants upstream due to inundation and downstream due to dam break flooding (Korup 2002; Zhou et al. 2013; Zhang et al. 2014). The dynamic movement of failure mass and formation mechanism of the landslide dam are key information in evaluation of possibility of dam break and emergency response preparation (Dunning et al. 2006; Shi et al. 2017). The speed, topography, and

sliding volume of failure mass are strongly linked to the formation and shape of the landslide dam (Cui et al. 2009). Further, the mass movement process is accompanied by a complicated interaction with underlying materials. Thus, the formation mechanism of the landslide dam is quite unclear and still under considerable debate (Dufresne 2012; Zhou et al. 2017). The source mass commonly disintegrates into landslide-debris avalanches due to collision and is likely to attain a high speed during the slide (Yang et al. 2011; Cui et al. 2019; Li et al. 2019). During the mass movement process, the high-speed landslide-debris avalanches impose a strong impact and traction force on the ground, and the basal entrainment and volume enlargement effects are pronounced, which can significantly affect the formation and shape of the landslide dam (Wang et al. 2003; Pudasaini and Krautblatter 2014).

In the early morning on October 11, 2018, a massive landslide suddenly occurred at the right bank of the Jinsha River at the junction area of Sichuan Province and Tibet, China (N: 31° 4′ 51″, E: 98° 43′ 01″) (Fig. 1a). The high-speed sliding mass rushed into and blocked the Jinsha river, and formed a large landslide dam (Fig. 1b). Due to the rapid rise in the water level behind the block, the landslide dam started to overflow naturally only 34 h after its formation, and the water dropped to a safe level in 5 days. Unexpectedly, a secondary landslide, which was initially estimated to have limited influences on the drainage of landslide dammed lakes, occurred 23 days later (October 11, 2018) and blocked the Jinsha River again.

The Baige landslide dam is a typical but uncommon case of a geological disaster in a mountainous area that blocked the Jinsha River twice by the first and second landslides. Combining field investigations, including sampling, unmanned aerial vehicle (UAV) technology, and remote sensing using high-resolution satellite images, the pre-failure kinematic features and triggering mechanism of the landslides are identified; the dynamic behavior of the mass movement and its interaction with underlying materials are studied, and the failure mechanism of the landslides and formation process of the landslide dam are analyzed and discussed. A flowchart of the implemented research methodology is shown in Fig. 2. The results presented in this paper can provide a reference for failure mechanism analysis of landslides and risk assessment for secondary disasters of abrupt geologic hazards.

Regional geological and geomorphological setting

The Baige landslide is located at the junction area of Baiyu County, Sichuan Province and Jiangda County, Tibet. As shown in Fig. 3a, the study area belongs to the freeze-thaw plateau area; the elevation of this area is mostly above 3000 m, and some ridges are over 4500 m (Ouyang et al. 2019). The landscape of the study area is composed of high mountains and deep valleys, and the highest valley shoulder height difference exceeds 1000 m. As shown in Fig.
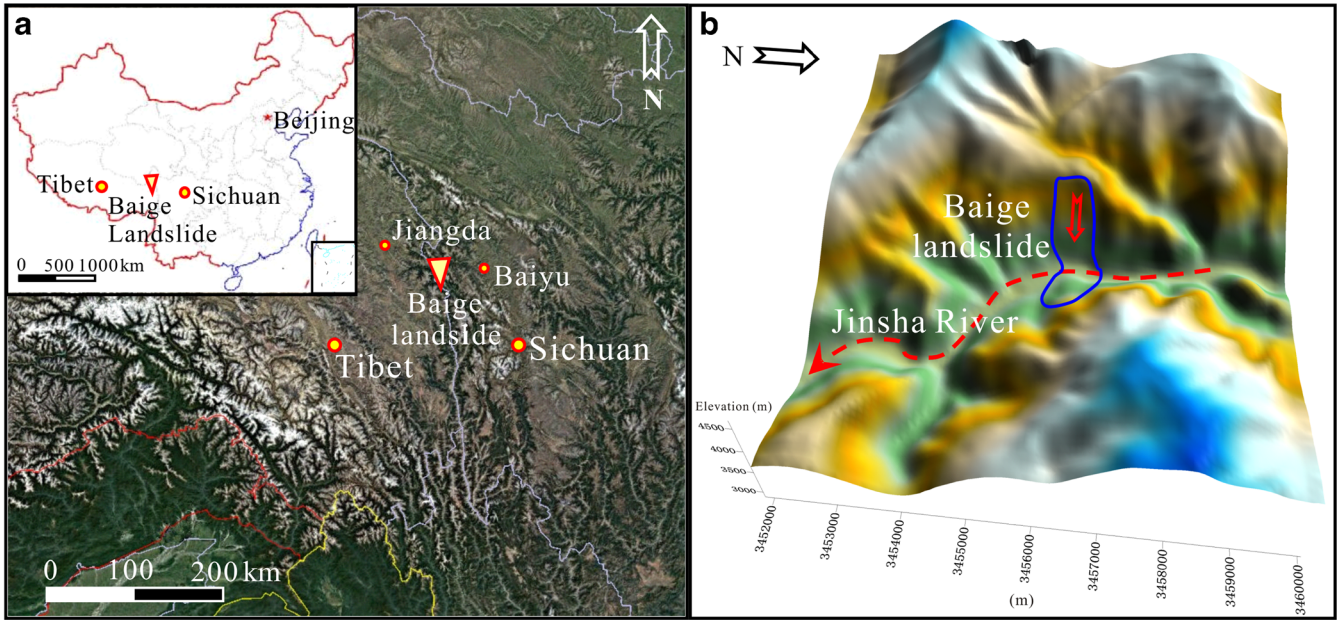
Fig. 1 Location of the Baige landslide: **a** location of the study area and **b** 3D view of the Baige landslide

3b, the regional geological setting is quite complex, and the strata are mainly composed of plagioclase gneiss ($P_t xn^a$), rock fragment sandstone ($T_3 jn$), granodiorite ($\gamma\delta_5^{2a}$), and serpentine ($\phi_{\omega4}$) (Xu et al. 2018). A series of NNW-trending faults or folds are developed in the study area, and the Boluo-muxie fault F_{14} (with a strike of N30°W, a dip direction of SW and a dip angle of 50°–70°) passes through the top of the landslide area along the mountain ridge.

The slopes at both banks are quite steep, with the slope gradient estimated at 30°–50° in the landslide area (Fig. 3c). The sloping area is covered with several to tens of meters of Quaternary loose accumulation bodies resulting from collapses, fluvial sediments and glacial deposits. The landslide area has outcrops of mainly plagioclase gneiss ($P_t xn^a$) and serpentine ($\phi_{\omega4}$). The rock strata mainly dip towards the mountain and downstream side, with a strike of N40°–50°W, a dip direction of SW and a dip angle of 45°–60°. Under long-term geological effects, the rock mass is characterized by low-angle folds or flexural deformation (Fig. 3d). Cracks are well developed because of weathering and unloading and are dominated by two groups of joints: group I is approximately parallel to the landslide surface with a strike of N330°–380°W, a dip direction of NE and a dip angle of 75°–85°; and group II is approximately vertical to the ridge line with a strike of N10°–25°W, a dip direction of SE and a dip angle of 80°.

As shown in Fig. 4, the field investigation indicated that the Baige landslide was a typical slope failure with a high-speed sliding mass, and the source mass slid down from the top of the mountain
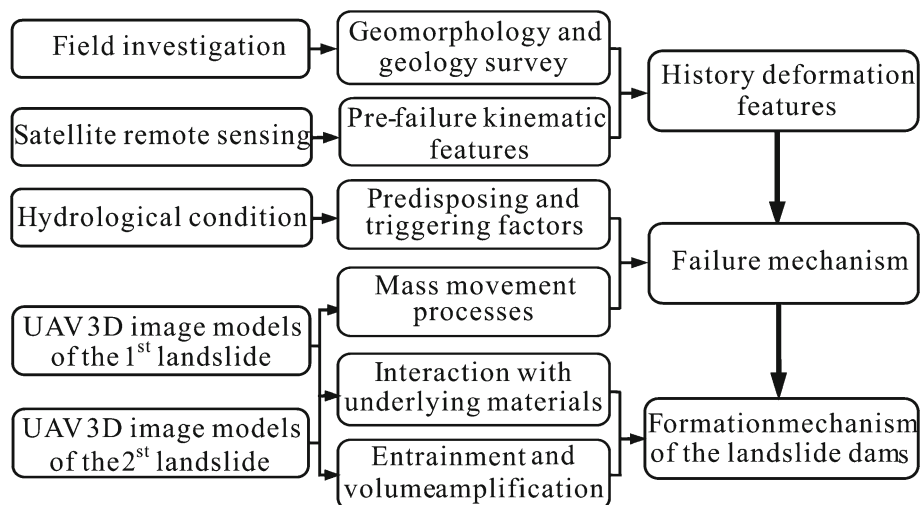

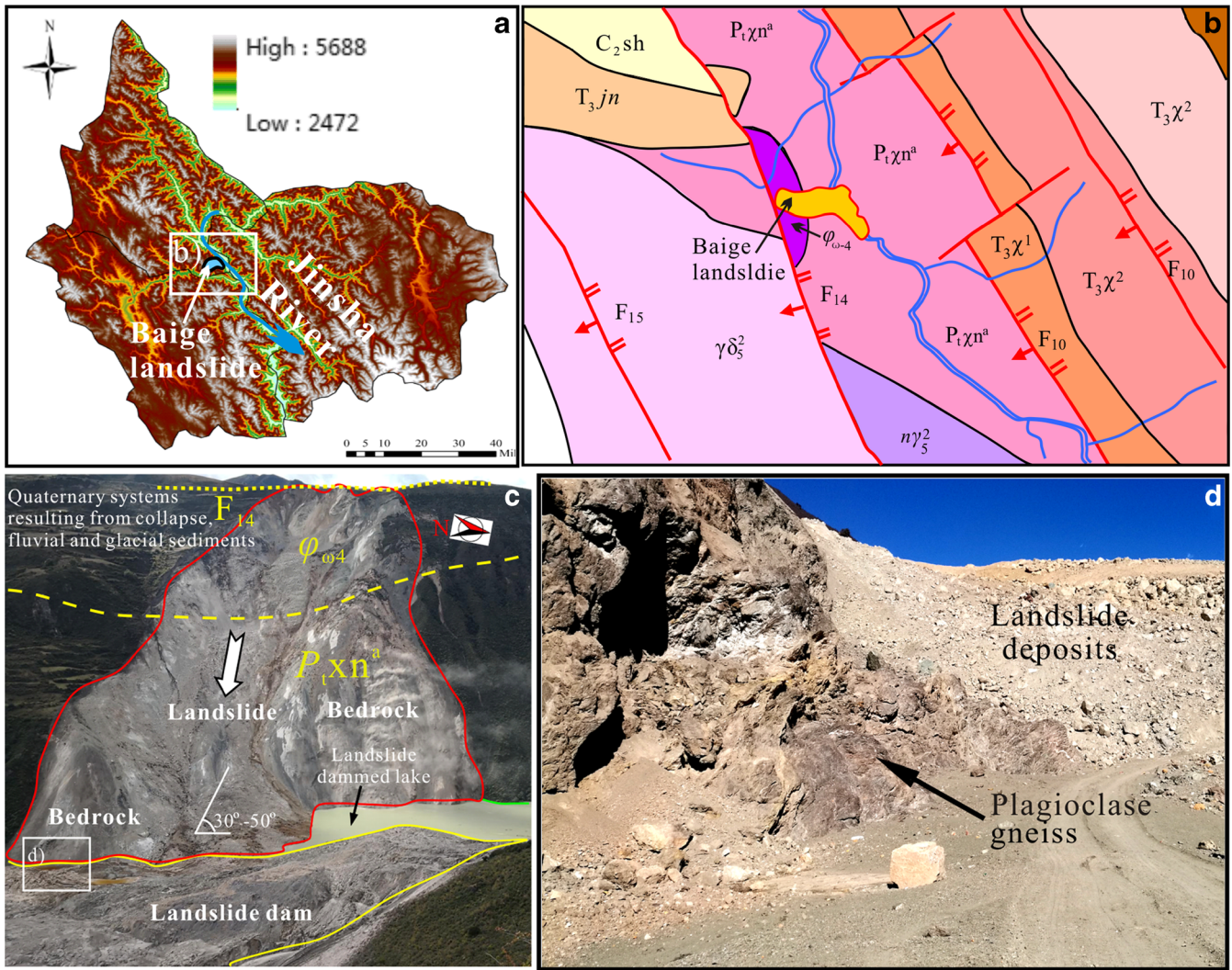**Fig. 2** Flowchart of the research methodology implementation

Fig. 3 Geomorphological and geological setting of the Baige landslide: **a** regional geomorphological setting; **b** geological map of the study area (after Xu et al. 2018); **c** field geology investigation result of the Baige landslide; and **d** local view of the landslide dam

ridge at an average elevation of more than 3720 m. The relative elevation difference exceeds 840 m, and the run-out distance was approximately 1500 m. Approximately 1.0×10^7 m³ of sliding mass rushed into the Jinsha River and caused a high surge of more than 150 m. The surge hit the river bank on the other side and swept away the trees and other vegetation, leaving a large scar with a height of 150–200 m and a length of more than 1000 m. The ensuing accumulation body from both banks blocked the river channel and formed the Baige landslide dam. The large landslide dam was estimated to have a volume of more than 1.5×10^7 m³ with an average height of 80 m and a length of 1100 m. The volume of the resulting landslide dammed lake was estimated to be more than 2.7×10^8 m³. The lake started overflowing 34 h later, and the water level dropped to a safe level of 2894.6 m 5 days later.

Unexpectedly, a secondary landslide occurred at the back edge of the remnant slope 23 days after the initial landslide. More than 6.0×10^6 m³ of sliding mass rushed into the natural spillway (formed during the previous overflow) and blocked the Jinsha River again. The total volume of the landslide dammed lake was

greatly enlarged and estimated to be more than 7.7×10^8 m³. A timely and appropriate manual intervention was imperative and necessary to decrease the water level, reduce the dam break risk, and minimize the economic losses. A drainage channel was excavated to discharge the lake water, and the dam break risk was totally removed 10 days later.

Failure mechanism analysis of the Baige landslide

Deformation history analysis

To investigate the deformation history of the Baige landslide, two scenes of remote-sensing images from Google Earth prior to the landslide (Fig. 5) were acquired and analyzed through visual interpretation (Fan et al. 2017). As shown in Fig. 5a, significant deformation can be observed since Mar. 4, 2011. Several small-scale collapses took place at the middle and back of the landslide area. Two tension cracks along the mountain ridge (CR_2 and CR_4) and three along the sliding direction (CR_1, CR_4, CR_4) could be identified at the back of the landslide area. Among these cracks,
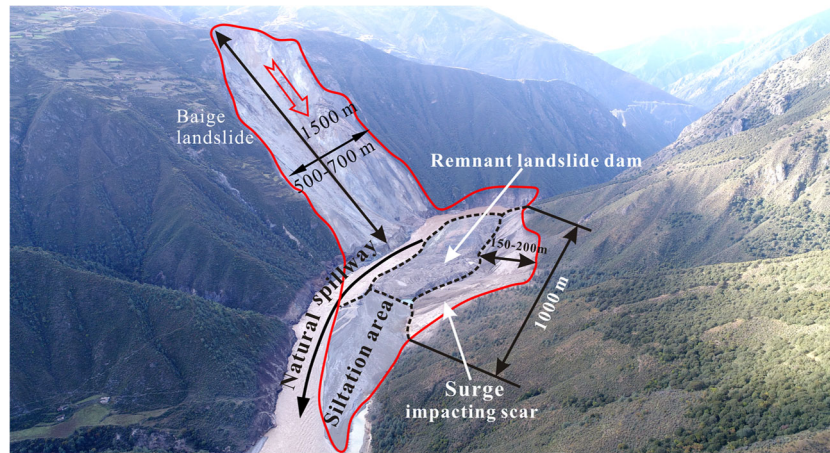
Fig. 4 Main geometric information of the Baige landslide

the longest crack (CR$_1$) zigzagged for 150–200 m with a visible staggered step of 6–10 m. The other cracks stretched to various sizes, and most were opened. Figure 5b shows an image of the potential landslide area on Feb. 22, 2015. It can be seen that the deformation and failure phenomenon intensified because of gravity, rainfall, or ice/snow melting. Small-scale sliding and collapses occurred more intensively with the cracks being deepened and widened. The stretch length and opening width of CR$_1$ were significantly enlarged, and its visible deformation dislocation increased to 10–15 m. Small-scale collapse was densely developed at the back of the landslide along CR$_2$ and CR$_4$. A remarkable deformation can be identified by comparing the positions of the paths (1–1 and 2–2) across the upper part of the landslide area. The increasing development of the cracks, small-scale collapses, and deformation phenomenon suggested that the potential failure mass had already been substantially deformed and was prone to massive failure.

Failure mechanism analysis

The Baige landslide was initiated by the combination of predisposing and triggering factors. Under the combined actions of topography, geology, and the physical and chemical effects of underground water, the slope was characterized by large creep deformation (Fig. 5). Ultimately, the change in hydrological conditions induced the avalanche.

The Baige landslide was located in a typical freeze-thaw plateau area, and the steep slope angle (30°–50°), strongly weathered rock mass, glaciers, and thick Quaternary deposits under the original ground surface were quite unfavorable to the stability of the slope. As shown in Fig. 3, the bedrock was mainly composed of plagioclase gneiss and serpentine, which are characterized by a relatively low mechanical strength and intense ductile shearing deformation behavior. Fault F$_{14}$ and the intensely developed cracks had a great impact on slope stability and promoted the deformation and cracking of the slope and facilitated the
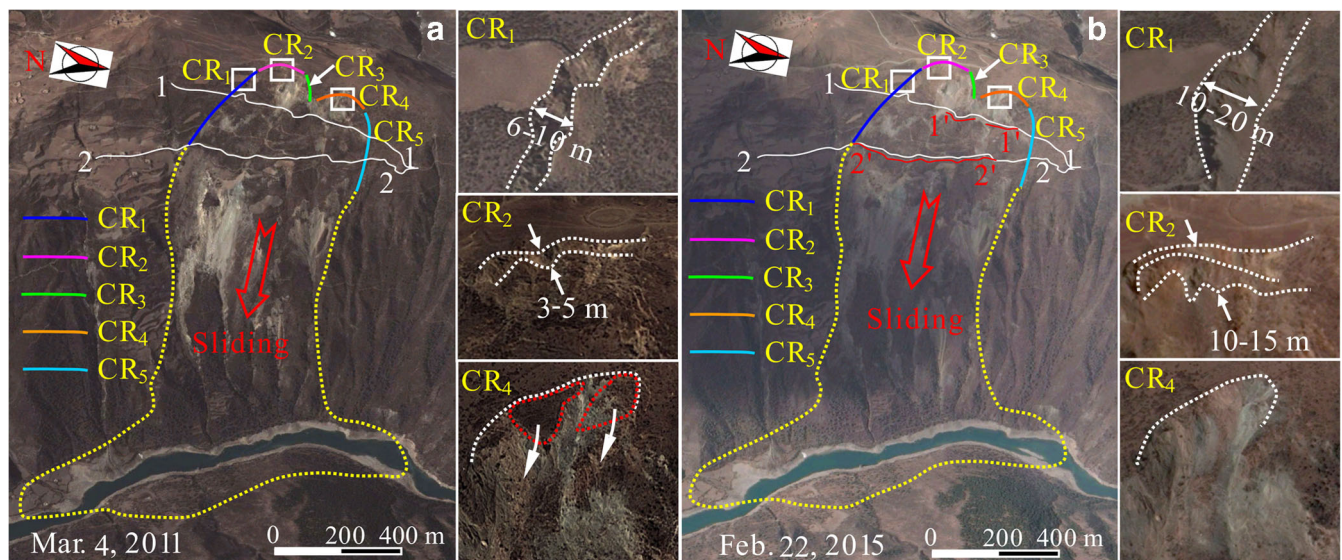

Fig. 5 Two scenes of remote-sensing images of the Baige landslide from Google Earth: **a** on Mar. 4, 2011, and **b** on Feb. 22, 2015
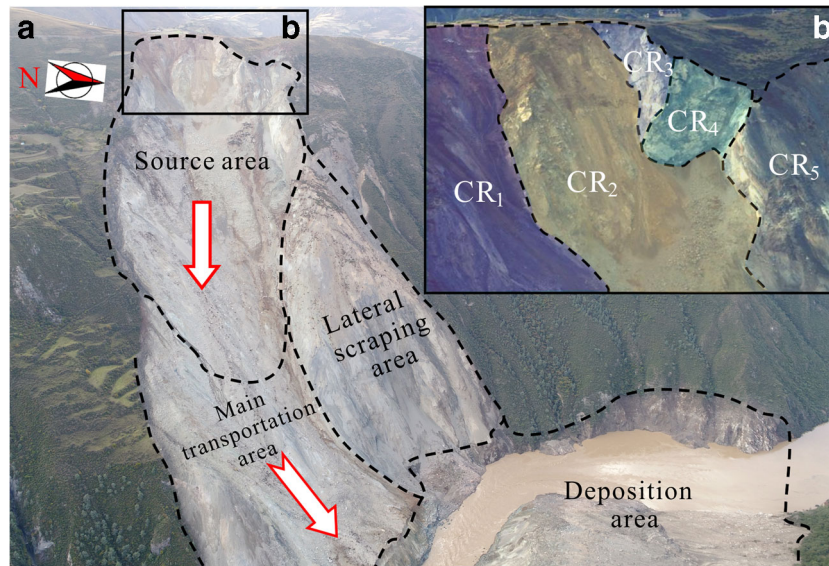
Fig. 6 High-resolution image of the landslide scar taken by the UAV: **a** a view of the landslide scar and **b** source area of the Baige landslide

basal sliding preceding the massive failure. The continuous development of cracks and fractures at the back of the landslide had an extremely adverse impact on the stability of the slope. Figure 6 shows a high-resolution image of the landslide scar taken by the UAV. As shown in Figs. 5 and 6, the cracks were well developed and bounded the source area of the landslide. CR_1 formed the southern edge, and CR_3, CR_4, and CR_5 formed the northern edge of the source area. CR_2 along the ridge of the slope developed into the slope for approximately 150–200 m and formed the main slip surface of the source area. The increasing development of creep deformation promoted rapid propagation and opening of preexisting cracks and likely contributed to the synchronous initiation, propagation, and coalescence of new microcracks in the bedrock (Stead and Wolter 2015; Li et al. 2018). Signs of weathering in the surface of CR_2 can be observed (Fig. 6b), suggesting significant rainwater infiltration, groundwater circulation, and erosion. Open cracks provided preferential paths for the infiltration of water and thus indirectly accelerated the physical and chemical weathering of the bedrock (Smith 2015; Segoni et al. 2018). Furthermore, the freeze-thaw cycle effect of the glacier could have accelerated crack expansion and caused adverse impacts on the slope. The gradual penetration of cracks formed the critical slip surface of the landslide, which had in turn increased the possibility of slope failure. The typical geological conditions in the source area of the landslide provided favorable conditions for the initiation of landslides. The progressive large deformation led to serious deformation and cracking of the buildings on the landslide area and forced the relocation of local residents. The field investigation and satellite remote sensing results indicate that the deformation and failure models of the Baige landslide are a combination of creep sliding and cracking at the surface and fracturing in the deep areas.

Persistent rain was the primary triggering factor for dramatic failure. As shown in Fig. 7, the Baige landslide area belongs to a typical mainland monsoon climate, and the rainfall displayed an uneven distribution over a year, mainly concentrated in the summer. Figure 7a shows that the mean annual precipitation was 626.6 mm, while almost 78% of precipitation occurred from June to September (487.5 mm). According to the nearby Baiyu National General Meteorological Station (approximately 20 km away from the site of the landslides), the accumulated rainfall over the past 4 months before the slide exceeded 590 mm, and the precipitation over the 10 days before the slide (in early October 2018) reached a value of 45.9 mm, which was obviously higher than the average rainfall rate observed over the same period in previous years (Fig. 7b). The Baige landslide was not induced by one particular heavy rainfall event but rather by the combination of the complex gravitational and hydrological effects over a relatively long time period. Regarding the long-term effect, prolonged rainfall infiltration would cause a slow but progressive build-up of hydrostatic pressures in the cracks, which might induce crack propagation and creep deformation (Fan et al. 2017). This effect led to crack propagation, which finally accelerated the infiltration rate as well as the creep deformation. In addition, persistent rainfall infiltration softens the rock mass and reduces the mechanical strength of both covering deposits and bedrock (Qi and Vanapalli 2015; Li et al. 2018). For the short-term effects, heavy rainfall resulted in the saturation of loose deposits on the surface and increasing pore water pressure on the structural surfaces. This effect led to crack propagation and accelerated deformation, which finally triggered catastrophic failure.

In regard to the failure mechanism of the Baige landslide, the complex geological conditions provided the necessary conditions for initiation of the landslide. Long-term gravitational and hydrological effects resulted in creep deformation and gradually deteriorated slope stability. Finally, the short-term heavy rainfall in early October 2018 triggered the dramatic failure through an increase in hydrostatic pressure.
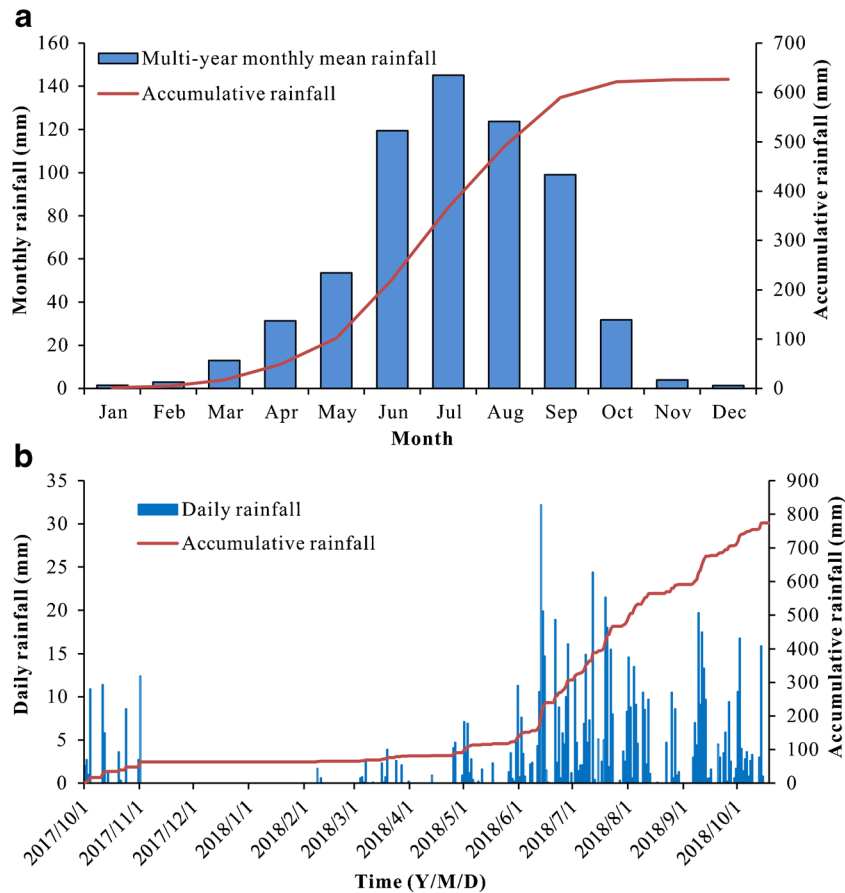
Fig. 7 Precipitation data of the study area (Baiyu National General Meteorological Station): **a** multiyear mean rainfall and **b** daily rainfall before the landslide

Mass movement and formation of the Baige landslide dams

Mass movement and overflowing of the "10.11" landslide dam

To investigate the landslide in detail, UAV technology was used to acquire high-resolution 3D image models of the Baige landslide (Fig. 8). According to the topography and geomorphology characteristics, the area influenced by the landslide can be generally divided into four major zones: the source area, the transportation area, the lateral scraping area, and the deposition area.

As shown in Figs. 6 and 8a, the source area was bounded by preexisting cracks, over which a remnant slope was formed with a steep angle ranging from 50° to 70° and a width of 200–400 m after the landslide. The rock mass was mechanically characterized by relatively low strength and structural fragmentation due to long-term weathering and unloading. The source mass detached from the top of the mountain ridge at an average elevation of more than 3720 m and extended to the middle lower part of the slope at an elevation of approximately 3000 m. Then, the landslide mass slid along the slip surface with a high kinetic energy, eroding the preexisting loose deposits by scraping. A wide (500–700 m) but short (200–600 m) scrape area was observed below the source area. According to the morphological characteristics, the scraped area can be divided into a U-shaped main transportation area and a triangle-shaped lateral scraped area. The main transportation area was extended along the main sliding direction, where the

majority of the failure mass passed through at high speeds. Because the lateral scraped area was eroded inadequately, where the original ground fragments can be observed in different locations, it was much shallower than the main transportation area.

As shown in Figs. 8a and 9a, the large sliding mass with entrained loose deposits was pushed down by the high gravitational energy towards the bank on the other side of the river (left bank), where a landslide dam with a sloping surface was formed quickly after the initiation of the landslide. The highest part of the landslide dam was approximately 115 m (elevation of 2985 m) on the left bank side, while the lowest elevation was approximately 2931 m (height of 61 m) on the right bank side (Fig. 9a). The landslide dam on the left side was mainly composed of rock blocks and was relatively stable, while the landslide dam on the right side was mainly composed of detritus and loose soil and was therefore in a less stable state.

As shown in Fig. 10a, the volume of the landslide dammed lake was estimated to be more than 2.7×10^8 m³, and the water level rose quickly after the landslide. Approximately 5.04×10^6 m³ of water flowed into the landslide dammed lake per hour, and the rate of rise in the water level is estimated to be 0.5–0.6 m per h. Fortunately, the sloping shape of the landslide dam provided a favorable condition for natural overflowing. More importantly, the dam break risk was estimated to be low, and no manual intervention was required because of the significant long length and gentle
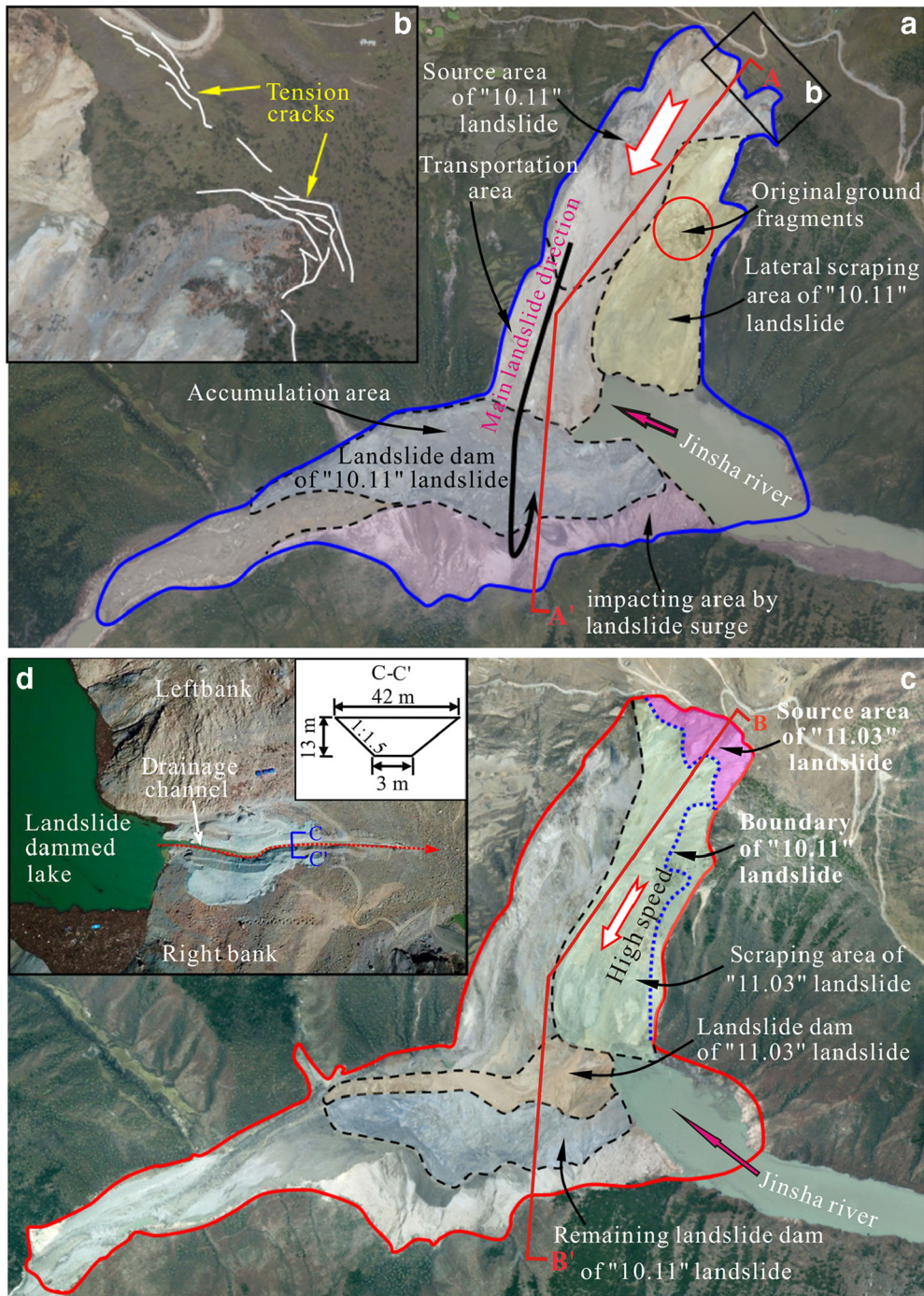
Fig. 8 High-resolution 3D image model of the "10.11" and "11.03" landslides taken by the UAV: **a** mass movement of the "10.11" landslide, **b** tension cracks at the back edge of the remnant slope after the "10.11" landslide, **c** mass movement of the "11.03" landslide, and **d** top view of the drainage channel of the "11.03" landslide dam during excavation

slope of the dam. At approximately 17:00 on October 12, 2018 (approximately 34 h the landslide), the landslide dam started overflowing. Until the early morning of Oct. 15, 2018, a natural spillway with a width of 100–120 m was formed, and then the water level behind the dam dropped continuously (Fig. 10b). By the end of Oct. 16, 2018, the water level dropped to 2894.6 m, and the risk of quick break of this dam was no longer present.

Formation and discharging of the "11.03" landslide dam

Due to the first landslide, a remnant slope with a steep angle of 50°–70° was formed. Large numbers of deep tension cracks were found along the back edge of the remnant slope due to the previous long-term creeping deformation and the unloading and stress adjustment effects caused by the "10.11" landslide. As shown in Fig. 8b, many large tension cracks can be identified at the back
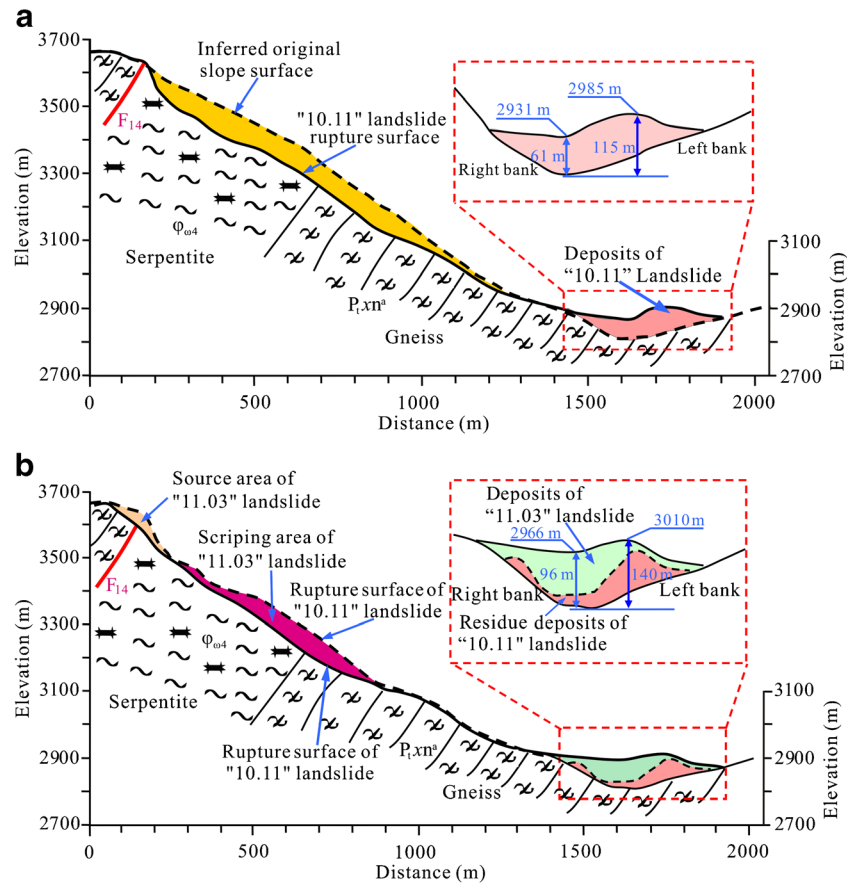
Fig. 9 Cross sections along the main sliding profile: **a** for the first landslide along location A-A′ and **b** for the second landslide along location B-B′

edge of the remnant slope through the high-resolution UAV image. These tension cracks, combined with other unfavorable conditions, such as interlaminar shear cracks and hydrostatic pressure formed by rainfall infiltration, had strongly affected the stability of the back edge of the remnant slope.

This area was assessed to be in poor condition in terms of stability, but the volume of the potential failure mass was initially estimated to be much lower than 2.0×10^6 m³ and to have little influence on the drainage of the landslide dammed lake. Unfortunately, a secondary landslide, with a significant volume of sliding mass, occurred at the back edge of the remnant slope at 17:00 on November 3, 2018, 23 days after the first landslide. As shown in Fig. 8c, the source area of the second landslide detached from the top of the mountain ridge at a high elevation of 3728 m with a volume estimated to be less than 2.0×10^6 m³. During the high-speed mass movement process, the sliding mass scratched and eroded the slope-wash, and the scraped area had been substantially widened and deepened. As a result, a total of more than 6.0×10^6 m³ of sliding mass, combined with loose deposits, rushed into the Jinsha River, blocked the original spillway and formed another landslide dam. The lowest height of the original landslide dam on the right bank side increased to a height of more than 96 m (elevation of approximately 2966 m), and the highest elevation on the left bank side also increased to 3010 m (Fig. 9b).

As shown in Fig. 10a, although the inflow decreased to approximately 2.92×10^6 m³ per hour and the water level rose by 0.22 m

per hour, the total volume of the landslide dammed lake was greatly enlarged and was estimated to be more than 7.7×10^8 m³ (water level of 2966 m). The probability of dam failure was particularly high if the water level rose to 2966 m and started overflowing without human intervention. In addition, the submerged range and the economic losses at the upstream and downstream areas would be extremely large. Therefore, a timely and appropriate manual intervention, such as excavating drainage channels to decrease the water level, was necessary and feasible.

A drainage channel was designed to discharge the lake water at the left bank side of the landslide dam. Until November 10, 2018, a trapezoidal drainage channel was excavated with a length of approximately 200–240 m, a bottom width of 3 m, and an average depth of 13 m (Fig. 8d). The water from the landslide dammed lake started to flow at approximately 10:00 on November 12, 2018. After 55 h of discharge, the water level dropped from the highest elevation of 2956.4 m down to 2898.4 m, and the dam break risk was totally removed.

Sliding volume amplification effect and accumulation analysis

Landslides are a typical geological disaster that can significantly affect the flow of mountainous rivers and induce secondary geological disasters (Pudasaini 2014; Stefanelli et al. 2016). Landslides with different sliding volumes will result in different secondary geological disasters (Chen and Chang 2016). A small-scale landslide may only have limited influence on the river flow, of which
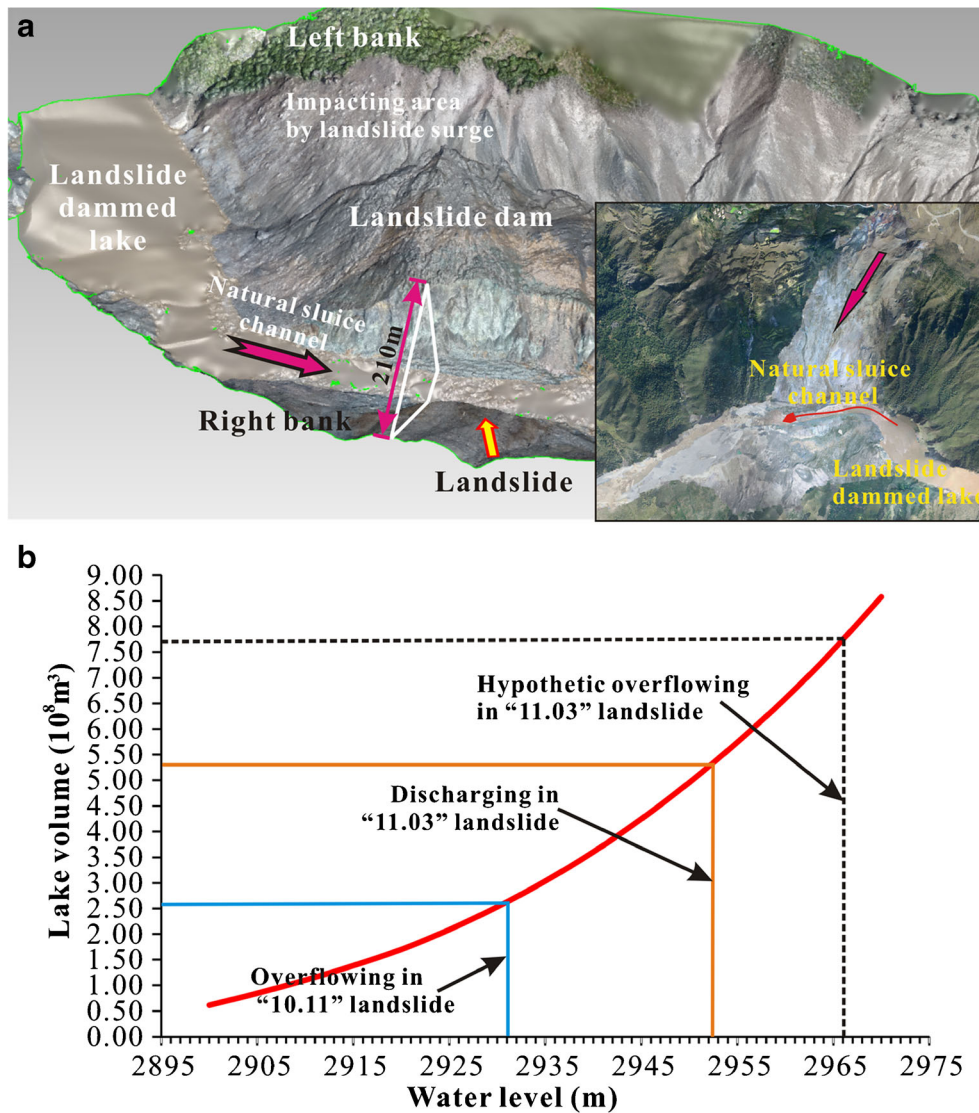
Fig. 10 Overflowing characteristics of the Baige landslide dams: **a** water level-lake capacity curve for the first and second landslide dammed lakes and **b** geometric information of the spillway

the sliding mass will be quickly carried away by the water flow (Pudasaini 2012). However, a large-scale landslide is very likely to block the river and form a landslide dam (Fan et al. 2012; Zhou et al. 2013).

The sliding volume is related not only to the source of the sliding mass but also to the scraping and entraining effects during the mass movement process, especially for high-speed landslides (Hungr and Evans 2004; McDougall and Hungr 2005). For example, the source volume of the failure mass of the Wenjiagou landslide triggered by the 2008 Wenchuan earthquake was estimated at approximately 2.7×10^7 m³, while the total accumulation volume in the gully was actually more than 5.0×10^7 m³ (Huang and Zhao 2010). Significant landslide entrainment and volume amplification were observed during the high-speed mass movement of the 2000 Yigong landslide in Tibet, China. The resulting accumulation volume was estimated to increase to 3.0×10^8 m³,

which blocked the main river by forming a large landslide dam (Zhou et al. 2016).

As shown in Fig. 9, for a detailed analysis of the scraping and entraining effects of the Baige landslides, two cross sections for the first and second landslides are made along the main sliding profile A-A′ and B-B′, respectively (Fig. 8 a and c). Due to the short sliding distance, the entrainment and sliding volume amplification effects are unobvious in the "10.11" landslide (Figs. 8a and 9a). However, notable scraping and entraining were observed during the mass movement for the second landslide on November 3, 2018, as a result of high-speed failure. As shown in Figs. 8c and 9b, the source mass detached from the top of the mountain ridge at a high elevation and slid down along the steep terrain at a high speed. The avalanche mass hit with very high kinetic energy on the original sliding bed, where massive loose deposits were accumulated by the "10.11" landslide. The sliding mass was fragmented and

transformed into a rock avalanche because of crashing and collision loading. During the high-speed mass movement process, the interaction with underlying materials was notable. Much of the bed deposit was impacted and scraped by the high-speed sliding mass. The original scraped area was substantially widened and deepened (Fig. 8c), and the original ground fragments on the lateral scraping area (Fig. 8a) were totally removed. The heavy rainfall in early October 2018 resulted in high water content or saturation of bed deposits and caused the entrainment to be more serious. When the high-speed sliding mass impacted the bed deposits, the pore water pressure rose rapidly, and the excess pore water pressure reduced the shear strength of the bed material and facilitated failure. The existence of water played a key role during the mass movement process of landslides, especially for the entrainment of landslides (Zhou et al. 2016). The scraping, eroding, and entraining on preexisting loose deposits greatly increased the sliding volume and expanded the scrape zone (Fig. 8c). The total volume of the resulting landslide deposition was estimated to be more than 6.0×10^6 m³, approximately three times that of the source mass volume.

The speed, topography, and sliding volume have significant effects on the accumulation and shape of the landslide dam. Due to the high speed of the first landslide, the deposits rushed towards the opposite bank, mainly accumulated at the left bank and formed a sloping-shaped landslide dam (the height of the dam at the right bank is much lower than that at the left bank, as shown in Fig. 9a). However, the rock mass of the second landslide on November 3, 2018, mainly accumulated at the toe of the slope (on the right bank side) because of the topography and obstruction from the remnant landslide dam body (Fig. 9b). The volume of the "11.03" landslide, which was initially estimated to be much lower than 2.0×10^6 m³ and considered to have little influence on the drainage of the landslide dammed lake, was significantly enlarged to more than 6.0×10^6 m³ from the entrainment and sliding volume amplification effects. Due to the volume and deposition status of the "11.03" landslide, the original sloping shape of the landslide dam has changed. The lowest height of the landslide dam was increased to more than 96 m with the corresponding volume of the landslide dammed lake estimated to be more than 7.7×10^8 m³ (Fig. 10a). As a result, the dam break risk was high, and a swift and aggressive treatment had to be taken to drain the water.

Stability analysis of the remnant slope

After the second landslide, myriad deep-seated cracks still existed along the back edge of the remnant slope. Due to terrain features and crack distribution characteristics, three potential unstable areas can be identified through the high-resolution 3D image model and field investigation: the K_1 zone, K_2 zone, and K_3 zone (Fig. 11).

The K_1 zone is along the back edge of the remnant slope. This zone has a length of approximately 400 m, a width between 30 and 60 m and a height of approximately 80–100 m, and its volume is estimated to be 1.5×10^6 m³. The strongly weathered rock mass in this area is broken with poor strength (Fig. 11c). Numerous large cracks can be observed through the high-resolution UAV images, and the majority of them are distributed in nearly south-north directions with steep dip angles. Most of the cracks are open with a
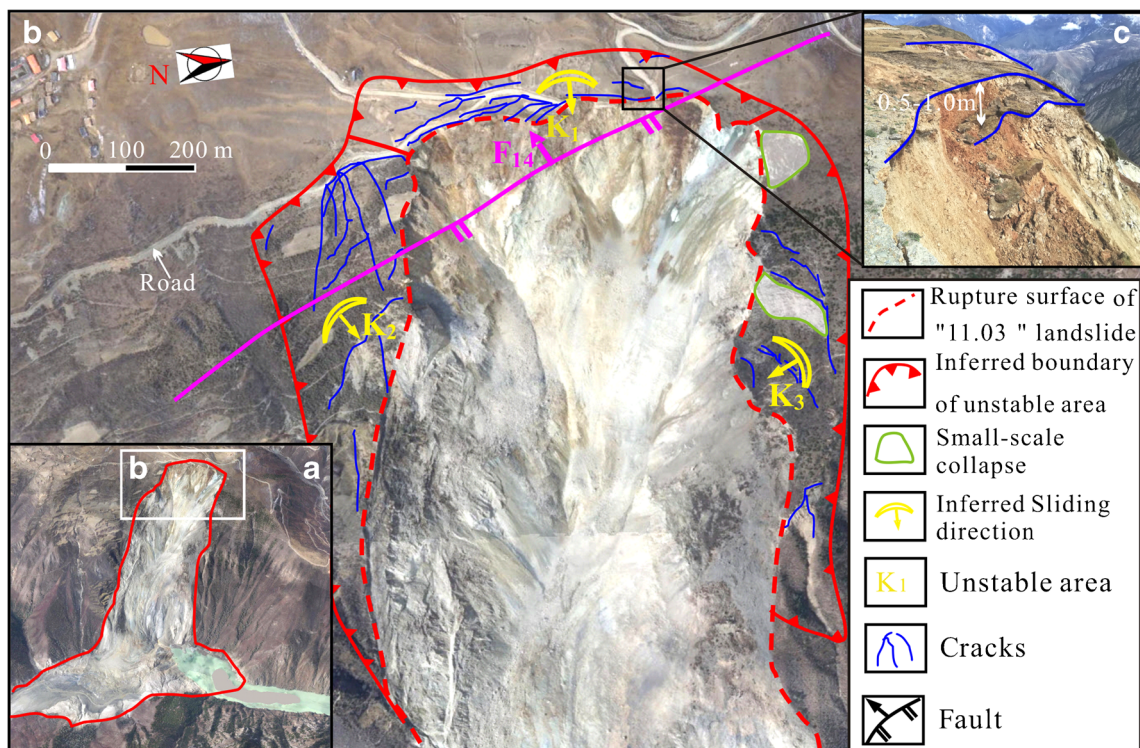

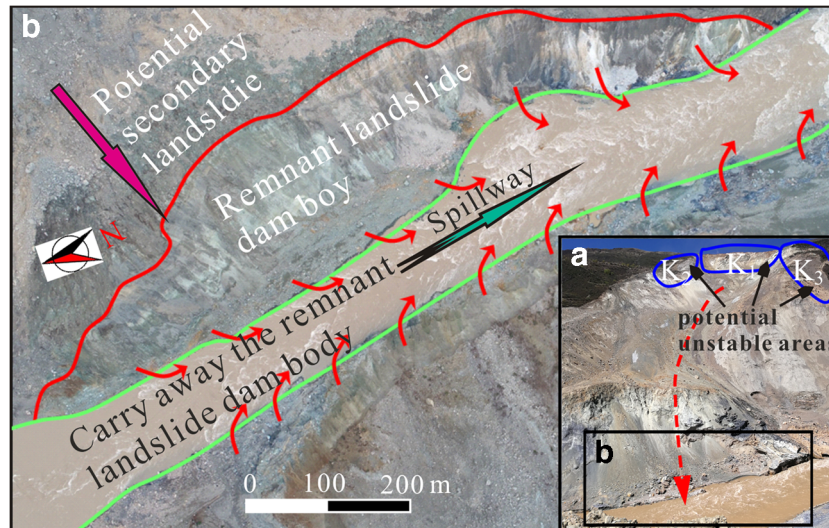**Fig. 11** Potential unstable area distributions on the remnant slope

Fig. 12 Method for taking advantage of the erosion and transportation features of the flow to carry away the remnant landslide dam body

width of 20–50 cm, a visible depth of 1.0–2.0 m, and a length of 10–100 m. Staggered steps can be obviously observed near the back edge of the remnant slope with a staggered distance of 0.5–1.0 m (Fig. 11c). The K_2 zone is triangle shaped at the south flank of the remnant slope. This zone has an estimated volume of 1.0×10^6 m^3 with a length, width, and thickness of approximately 800 m, 50–200 m, and 50–100 m, respectively. Tens of large open cracks are developed along the lateral edge or along the road at the top of the slope. The K_3 zone lies at the north flank of the remnant slope with an estimated volume of 1.2×10^6 m^3. Several small-scale collapses occurred in this area, and the outcrop rock mass was mainly composed of highly weathered serpentine.

After the first and second landslides, the stress state of the slope changed. During the unloading and stress adjustment process, new cracks emerged and expanded as a result of the shear stress concentration. Due to the gravitational effect, potential unstable areas gradually deformed towards the free surface and, in turn, promoted propagation and opening of the cracks. The continuous development of cracks and fractures at the back edge of the remnant slope had an extremely adverse impact on the stability of potentially unstable areas. Open cracks provided preferential paths for infiltration of water and thus increased the pore water pressure, softened the rock mass, and reduced rock mass mechanical indicators. The risk of potential unstable areas is prominent under unfavorable conditions, such as ice/snow melting, rainstorms, and earthquakes. These conditions pose a significant threat to the spillway of the landslide dam and may block the Jinsha River again. Hence, deformation monitoring and comprehensive treatment measures must be taken to reduce potential secondary disasters.

Discussion and conclusions

The Baige landslide dam is a typical case of a geological disaster in a mountainous area that blocked the Jinsha River twice via the first and second landslides. The two occurrences of landslides significantly increased the volume and height of compound landslide dam, with the volume amplification effect. Overflowing was not possible without manual excavation; the substantial volume of the landslide dammed lake posed a great threat to the towns and infrastructure in the upstream and downstream areas.

Combining the field investigation and UAV technology, the landslides characteristics and formation mechanism of the landslide dam are analyzed. The deformation and failure models of the first Baige landslide are the consequence of long-term creeping sliding, fracturing in the deep area under gravitational effect. Eventually, a short-term heavy rainfall triggered dramatic failure through an increase in hydrostatic pressure.

The formation of the "10.11" and "11.03" landslide dams suggested that the risk assessment for secondary disaster of a landslide is not an easy task. The speed, topography, and sliding volume have significant effects on the formation and shape of the landslide dam. The sliding volume is related not only to the volume of source material but also to the interaction with underlying materials during the mass movement process. It is difficult to accurately estimate the sliding volume and forecast the formation and shape of the landslide dam, particularly for high-speed landslides. The apparent effects of scraping, eroding, and entraining on preexisting loose deposits greatly increased the sliding volume and expanded the scrape zone. The heavy rainfall in early October 2018 resulted in high water content or saturation of bed deposits and caused the interaction to be more complicated. The ultimate sliding volume can be several times its initial size as a result of entrainment and volume amplification. Moreover, the topography and underlying surface conditions of the accumulation area have a significant effect on the formation and shape of the landslide dam, which should be considered carefully in the risk assessment of the secondary disaster.

Thus, the devastating consequences from multiple landslides can be unexpectable; timely measures should be carried out to reduce the associate risks, particularly, when the remnant slope is likely to fail again for this case (Fig. 11). For example, manually excavating the dam body and taking advantage of the erosion and transportation features of the flow to carry away the remnant

landslide dam body should be performed. This can make sufficient space for the mass of a possible third secondary landslide (Fig. 12).

References

Chen CY, Chang JM (2016) Landslide dam formation susceptibility analysis based on geomorphic features. Landslides 13(5):1019–1033

Costa JE, Schuster RL (1988) The formation and failure of natural dams. Geol Soc Am Bull 100(7):1054–1068

Cui P, Zhu YY, Han YS, Chen XQ, Zhuang JQ (2009) The 12 May Wenchuan earthquake induced landslide lakes: distribution and preliminary risk evaluation. Landslides 6(3):209–223

Cui Y, Cheng D, Choi CE, Jin W, Lei Y, Kargel JS (2019) The cost of rapid and haphazard urbanization: lessons learned from the Freetown landslide disaster. Landslides 16(6):1167–1176

Dufresne A (2012) Granular flow experiments on the interaction with stationary runout path materials and comparison to rock avalanche events. Earth Surf Process Landf 37(14):1527–1541

Dunning SA, Rosser NJ, Petley DN, Massey CR (2006) Formation and failure of the Tsatichhu landslide dam, Bhutan. Landslides 3(2):107–113

Fan X, van Westen CJ, Xu Q, Gorum T, Dai F (2012) Analysis of landslide dams induced by the 2008 Wenchuan earthquake. J Asian Earth Sci 57:25–37

Fan X, Xu Q, Scaringi G, Dai L, Li W, Dong X, Havenith HB (2017) Failure mechanism and kinematics of the deadly June 24th 2017 Xinmo landslide, Maoxian, Sichuan, China. Landslides 14(6):2129–2146

Huang HQ, Zhao QH (2010) Basic charactoristic and preliminary machanism analysis of large scale rockslide-sturzstrom at Wenjiagou triggered by Wenchuan. J Eng Geol 18(2):168–177 (in Chinese)

Hungr O, Evans SG (2004) Entrainment of debris in rock avalanches: an analysis of long run-out mechanism. Geol Soc Am Bull 116(9–10):1240–1252

Korup O (2002) Recent research on landslide dams-a literature review with special attention to New Zealand. Prog Phys Geogr 26(2):206–235

Li HB, Li XW, Ning Y, Jiang SF, Zhou JW (2018) Dynamical process of the Hongshiyan landslide induced by the 2014 Ludian earthquake and stability evaluation of the back scarp of the remnant slope. Bull Eng Geol Environ 78:2081–2092. https://doi.org/10.1007/s10064-018-1233-6

Li HB, Li XW, Li WZ, Zhang SL, Zhou JW (2019) Quantitative assessment for the rockfall hazard in a post-earthquake high rock slope using terrestrial laser scanning. Eng Geol 248:1–13

McDougall S, Hungr O (2005) Dynamic modelling of entrainment in rapid landslides. Can Geotech J 42(5):1437–1448

Ouyang C, An H, Zhou S, Wang Z, Su P, Wang D, Su P, Wang D, Cheng D, She J (2019) Insights from the failure and dynamic characteristics of two sequential landslides at Baige village along the Jinsha River, China. Landslides 16(7):1397–1414 1–18

Pudasaini SP (2012) A general two-phase debris flow model. J Geophys Res Earth Surf, 117(F3)

Pudasaini SP (2014) Dynamics of submarine debris flow and tsunami. Acta Mech 225:2423–2434

Pudasaini SP, Krautblatter M (2014) A two-phase mechanical model for rock-ice avalanches. J Geophys Res 119:2272–2290

Qi S, Vanapalli SK (2015) Hydro-mechanical coupling effect on surficial layer stability of unsaturated expansive soil slopes. Comput Geotech 70:68–82

Segoni S, Piciullo L, Gariano SL (2018) A review of the recent literature on rainfall thresholds for landslide occurrence. Landslides 15(8):1483–1501 1–19

Shi ZM, Xiong X, Peng M, Zhang LM, Xiong YF, Chen HX, Zhu Y (2017) Risk assessment and mitigation for the Hongshiyan landslide dam triggered by the 2014 Ludian earthquake in Yunnan, China. Landslides 14(1):269–285

Smith JV (2015) Self-stabilization of toppling and hillside creep in layered rocks. Eng Geol 196:139–149

Stead D, Wolter A (2015) A critical review of rock slope failure mechanisms: the importance of structural geology. J Struct Geol 74:1–23

Stefanelli CT, Segoni S, Casagli N, Catani F (2016) Geomorphic indexing of landslide dams evolution. Eng Geol 208:1–10

Xu Q, Zheng G, Li WL, He CY, Dong XJ, Guo C, Feng WK (2018) Study on successive landslide damming events of Jinsha River in Baige Village on Octorber 11 and November 3, 2018. J Eng Geol 26(6):1534–1551 in Chinese

Yang Q, Cai F, Ugai K, Yamada M, Su Z, Ahmed A (2011) Some factors affecting mass-front velocity of rapid dry granular flows in a large flume. Eng Geol 122:249–260

Wang G, Sassa K, Fukuoka H (2003) Downslope volume enlargement of a debris slide–debris flow in the 1999 Hiroshima, Japan, rainstorm. Eng Geol 69:309–330

Zhang LM, Zhang S, Huang RQ (2014) Multi-hazard scenarios and consequences in Beichuan, China: the first five years after the 2008 Wenchuan earthquake. Eng Geol 180:4–20

Zhou JW, Cui P, Hao MH (2016) Comprehensive analyses of the initiation and entrainment processes of the 2000 Yigong catastrophic landslide in Tibet, China. Landslides 13:39–54

Zhou J, Cui P, Fang H (2013) Dynamic process analysis for the formation of Yangjiagou landslide-dammed lake triggered by the Wenchuan earthquake, China. Landslides 10(3):331–342

Zhou JW, Yang XG, Hou TX (2017) An analysis of the supply process of loose materials to mountainous rivers and gullies as a result of dry debris avalanches. Environ Earth Sci 76(13):452

H.-b. Li · S.-c. Qi · J.-w. Zhou (✉)
State Key Laboratory of Hydraulics and Mountain River Engineering,
Sichuan University,
Chengdu, 610065, People's Republic of China
Email: jwzhou@scu.edu.cn

H. Chen
Sichuan Water Resources and Hydroelectric Investigation & Design Institute,
Chengdu, 610072, People's Republic of China

H.-m. Liao
College of Water Resource and Hydropower,
Sichuan University,
Chengdu, 610065, People's Republic of China

Y.-f. Cui
Department of Civil and Environmental Engineering,
Hong Kong University of Science and Technology, Clear Water Bay,
Hong Kong, People's Republic of China